Perovskite Phases

Deutsche Ausgabe: DOI: 10.1002/ange.201603835
Internationale Ausgabe: DOI: 10.1002/anie.201603835

Vacancy-Induced Electronic Structure Variation of Acceptors and Correlation with Proton Conduction in Perovskite Oxides

*Hye-Sung Kim, Ahreum Jang, Si-Young Choi, WooChul Jung, and Sung-Yoon Chung**

Abstract: *In most proton-conducing perovskite oxides, the electrostatic attraction between negatively charged acceptor dopants and protonic defects having a positive charge is known to be a major cause of retardation of proton conduction, a phenomenon that is generally referred to as proton trapping. We experimentally show that proton trapping can be suppressed by clustering of positively charged oxygen vacancies to acceptors in $BaZrO_{3-\delta}$ and $BaCeO_{3-\delta}$. In particular, to ensure the vacancy–acceptor association is effective against proton trapping, the valence electron density of acceptors should not significantly vary when the oxygen vacancies cluster, based on the weak hybridization between the valence d or p orbitals of acceptors and the 2p orbitals of oxygen.*

Among many notable physical properties and transport phenomena observed in perovskites,[1–3] aspects of high proton conductivity have been intensively investigated in zirconates and cerates over the past three decades[4–9] in efforts to elucidate the precise conduction mechanisms and further improve the ionic conductivity for real applications as electrolytes in solid-oxide fuel cells.[10] To easily incorporate protons into the perovskite lattice in the form of hydroxyl groups, $OH^{\bullet}$, negatively charged acceptors, A′, are usually doped through substitution for the Zr and Ce sites in zirconates and cerates[11] (the superscripts in $OH^{\bullet}$ and A′ are the Kröger–Vink notations). Therefore, the positively charged hydroxyl groups are electrostatically attracted by the negatively charged acceptors in the crystals, resulting in binding behavior between the two species.[12]

Theoretical calculations based on both the ab initio density-functional theory (DFT) and the empirical interatomic potentials have previously demonstrated that $OH^{\bullet}$ is energetically more favorable when it is bound to A′.[13–15] Furthermore, a recent study has provided notable experimental evidence of the proton–acceptor association, which is referred to as proton trapping, through systematic analyses based on thermogravimetry, nuclear magnetic resonance, and impedance spectroscopy.[16] It is thus generally accepted that proton trapping is a major obstacle to the long-range rapid conduction of protons inside single crystalline grains.

Previous reports have showed that the concentration of $OH^{\bullet}$ that can be incorporated into the lattice by a hydration reaction at 500–700 °C is approximately 3–6 mol % in acceptor-doped perovskite oxides.[17] As a result, a substantial amount of oxygen vacancies ($V_O^{\bullet\bullet}$) remains without filling by OH. As suggested very recently,[18] if oxygen vacancies clusters nearby acceptors, their positive charge can effectively cancel out the negative charge from the acceptors. The strong electrostatic attraction exerted by the acceptors to protons thus may be significantly reduced. In this work, taking two proton-conducting perovskites, $BaZrO_3$ and $BaCeO_3$, with three different acceptor dopants, In^{3+}, Y^{3+}, and Sc^{3+}, as model systems, we demonstrate that proton trapping can be remarkably alleviated when oxygen vacancies neighbor acceptors. However, it is noted that not all of the trivalent cations show identical behavior. More importantly, for oxygen vacancies to actively contribute to reducing proton trapping, the valence electron density of acceptors should be nearly invariable when oxygen vacancies cluster. Details for the experiments and calculations are provided in the Supporting Information.

First, we carried out DFT calculations to theoretically compare the electron density difference before and after oxygen-vacancy formation. Figure 1 shows the fields of electron-density difference in the *c* projection for three different trivalent acceptors, In^{3+}, Y^{3+}, and Sc^{3+}. While the density difference does not significantly vary for In, that of Y and Sc substantially changes by the presence of an oxygen vacancy, as indicated by an arrow in each of the cases. Furthermore, when a vacancy forms, the angles of O–Y–O (101.2°) and O–Sc–O (99.8°) become larger than the O–In–O angle (96.5°). These distinct variations in both the electron-density difference and the angle induced by the oxygen vacancy in Y and Sc imply a notable redistribution of valence electrons. In fact, as numerically represented in Figure 1, a distinctively large reduction in the Mulliken charge[19,20] is noted in both Y and Sc (more than 20 %) in contrast to that of In (see the Supporting Information, Table S1 for specific values of the Mulliken charge from the electronic population analysis), directly indicating that Y and Sc become comparatively strong acceptors with higher negativity when an oxygen vacancy clusters.

The distinct behavior of electron-density redistribution by the oxygen-vacancy formation in the three acceptor dopants shown in Figure 1 can be understood by considering the

[*] H.-S. Kim, Prof. S.-Y. Chung
Graduate School of EEWS
Korea Advanced Institute of Science and Technology (KAIST)
Daejeon 34141 (Korea)
E-mail: sychung@kaist.ac.kr
nalphates@gmail.com
Homepage: https://sites.google.com/site/atomicscaledefects/
A. Jang, Prof. W. Jung
Department of Materials Science and Engineering
Korea Advanced Institute of Science and Technology (KAIST)
Daejeon 34141 (Korea)
Dr. S.-Y. Choi
Korea Institute of Materials Science
Changwon 51508 (Korea)

Supporting information for this article can be found under: http://dx.doi.org/10.1002/anie.201603835.

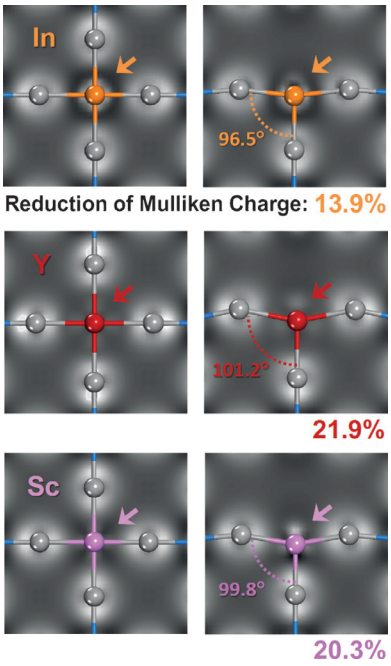

Figure 1. Fields of electron-density difference before and after oxygen-vacancy formation. For the three acceptor dopants, variations in electron density are schematically described along with the changes of the Milliken charge and the angle of the bond. While the electron density around In does not considerably vary with the formation of an oxygen vacancy, Y and Sc show a remarkable change in electron density.

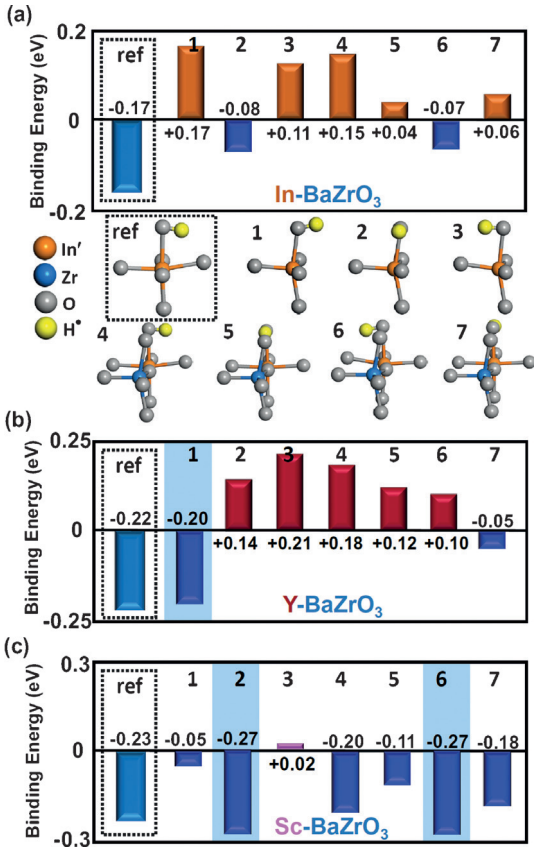

Figure 2. DFT calculation results for the OH•–A′ binding energy, ΔE_B, in $BaZrO_3$. a)–c) The bar graphs show the values of ΔE_B for In, Y, and Sc in $BaZrO_3$. Geometrically optimized $[InO_6]$ octahedra with OH• are also illustrated in (a). As denoted by "ref", the reference ΔE_B is presented for each of the three dopants, when OH• is bound to A′ without $V_O^{\bullet\bullet}$. Note that Cases 1–3 indicate the $[A'V_O^{\bullet\bullet}O_5]$ octahedra with OH• and Cases 4–7 represent the $[A'O_6]$–$[ZrV_O^{\bullet\bullet}O_5]$ with OH•. The sky-blue shadows in (b) and (c) indicates the binding energies that are comparable with the references.

partial density of states (PDOS) in the upper valence band. The O 2p orbitals are strongly hybridized with the Zr 4d orbitals in the $[ZrO_6]$ octahedra, constituting the major electronic states in the upper valence band (Supporting Information, Figure S1a). This hybridization between O 2p orbitals and 3d or 4d orbitals of transition metals in insulating perovskite oxides is typically observed bonding behavior.[21] Similarly, when Y and Sc are doped in $BaZrO_3$, a significant number of states from Y 4d and Sc 3d orbitals for hybridization with the O 2p orbitals can be verified. In strong contrast, there is no noteworthy orbital contribution from In in the valence band (Supporting Information, Figure S1b). Most of the $4d^{10}$ electron states of In were placed in a much lower valence band in the PDOS plot (Supporting Information, Figure S2). This notably weak hybridization with the O 2p orbitals directly indicates that the electron density of In would not be seriously affected by whether oxygen vacancies form in the $[InO_6]$ frame, providing excellent agreement with the nearly invariant electron-density difference shown in Figure 1.

We examined the influence of oxygen vacancies on the proton-acceptor binding energies through DFT calculations for the three dopants. The bar graphs shown in Figure 2a–c represent each of the OH•–A′ binding energies (A = In, Y, and Sc) obtained from the calculations in $BaZrO_3$. Herein, the binding energy (ΔE_B) is defined as the difference in lattice enthalpy, $\Delta E_B = E_{bound} - E_{sep}$, when A′ and OH• are separate from each other (E_{sep}) and bound as neighbors (E_{bound}). Each of the $[InO_6]$ octahedra having OH• from the geometrically optimized supercells is also illustrated in Figure 2a as examples of the seven different configurations between A′, $V_O^{\bullet\bullet}$, and OH•. Cases 1–3 represent the $[A'V_O^{\bullet\bullet}O_5]$ octahedral configurations and Cases 4–7 indicate the $[A'O_6]$–$[ZrV_O^{\bullet\bullet}O_5]$ with OH•. The most notable feature in this series of DFT calculations is that the binding characteristics between OH• and In′ significantly diminish when $V_O^{\bullet\bullet}$ is involved as a neighbor to In′. As shown in Figure 2a, the OH•–In′ binding energy in a $[InO_6]$ octahedron of $BaZrO_3$ is −0.17 eV. In contrast, this negativity of the binding energy is reduced and even changes to a positive value when $V_O^{\bullet\bullet}$ is incorporated in the $[InO_6]$ octahedron as $[InV_O^{\bullet\bullet}O_5]$ (Cases 1–3; ΔE_B ranges from −0.08 to +0.17 eV) and also when it places in an adjacent $[ZrO_6]$ octahedron as $[InO_6]$–$[ZrV_O^{\bullet\bullet}O_5]$ (Cases 4–7; ΔE_B ranges from −0.07 to +0.15 eV). The optimized geometry of OH• also was found to vary, depending on whether $V_O^{\bullet\bullet}$ is involved in the $[InO_6]$ octahedron. While the OH• group is slightly oriented toward In′ without $V_O^{\bullet\bullet}$, the angle of In–O–H becomes greater when $V_O^{\bullet\bullet}$ neighbors In′ (Supporting Information, Figure S3), reflecting the repulsion

between $OH^{\bullet}$ and $V_O^{\bullet\bullet}$. The $V_O^{\bullet\bullet}$–In′ clusters were also identified to be remarkably beneficial to reduce proton trapping in $BaCeO_3$. The detailed DFT results in $BaCeO_3$ and its crystal structure are provided in the Supporting Figures S4 and S5, respectively.

In contrast to the In dopant, binding between Y (or Sc) and protons does not appear to sensitively vary when oxygen vacancies are involved. Although the $OH^{\bullet}$–Y′ binding energy shows even positive values in Cases 2–6 for Y (Figure 2b), a negative binding energy (−0.20 eV), which is comparable that of the [YO_6] reference (−0.22 eV), is obtained in Case 1, indicating that strong trapping of protons is very likely to occur during their rotational motion at elevated temperature. Similarly, as denoted by sky blue shadows, highly negative binding energies in Cases 2 and 6 (−0.27 eV) for Sc are also presented in Figure 2c. Based on this series of DFT calculations for the binding energies, the $V_O^{\bullet\bullet}$–A′ defect association for Y and Sc is thus not believed to be as efficient as that for In in terms of suppression of $OH^{\bullet}$–A′ binding. Note that the results in Figure 2a–c are consistent with the variations of the Mulliken charge of the acceptors demonstrated in Figure 1. If the effective charge of acceptors becomes more negative by the oxygen-vacancy formation, as shown in Y and Sc, the positively charged $V_O^{\bullet\bullet}$ from the $V_O^{\bullet\bullet}$–A′ association cannot play an active role in suppressing the attraction of protons to acceptors (see the Supporting Information, Figure S6 for representational illustrations).

$BaZrO_3$ and $BaCeO_3$ ceramics are usually fabricated by sintering at high temperatures above 1600 °C for $BaZrO_3$ and 1400 °C for $BaCeO_3$. As a result, oxygen vacancies in acceptor-doped $BaZrO_3$ and $BaCeO_3$ distribute over the crystals in a random manner owing to the temperature-driven high entropy effect even if there is electrostatic attraction between $V_O^{\bullet\bullet}$ and A′. Table S2 in Supporting Information lists the $V_O^{\bullet\bullet}$–A′ clustering enthalpies, $\Delta E_{Clus} = E_{bound} - E_{sep}$ (where E_{sep} and E_{bound} are the lattice enthalpies with $V_O^{\bullet\bullet}$ separate from A′ and with $V_O^{\bullet\bullet}$ bound right to A′, respectively) for both $BaZrO_3$ and $BaCeO_3$. As already reported for other acceptor dopants in perovskite oxides,[13,14] the $V_O^{\bullet\bullet}$–A′ clustering enthalpies are also consistently negative (Supporting Information, Table S2), confirming that the cluster between $V_O^{\bullet\bullet}$ and A′ is energetically favorable. To maximize the clustering behavior and simultaneously minimize the entropy contribution, lowering the fabrication temperature is indispensable. Based on this thermodynamic consideration, we adopted an additional post-annealing process at much lower temperature after high-temperature sintering, providing sufficient time for oxygen vacancies to diffuse toward A′ and thereby to form $V_O^{\bullet\bullet}$–A′ clusters. Our DFT calculations in $BaZrO_3$ show that the diffusion activation energy of O via a vacancy mechanism has the lowest value among the activation energies of the three constituents (1.1 eV for O, 6.4 eV for Zr, and 4.2 eV for Ba), in excellent agreement with experimental results (0.89–1.0 eV for O) in a previous report[17] (Supporting Information, Figure S7). Furthermore, the diffusivities of oxygen vacancies in $BaZrO_3$ at 1300 °C and in $BaCeO_3$ at 1100 °C are on the order of about 10^{-5}–10^{-4} $cm^2 s^{-1}$.[5] Therefore, post-annealing at properly lower temperature for a sufficient time is a reasonable and efficient way of facilitating the diffusion of oxygen vacancies at a several-nanometer scale for the formation of $V_O^{\bullet\bullet}$–A′ clusters.

Before measuring the proton conductance of samples for comparison, we selected In-doped $BaZrO_3$ to visualize the presence of $V_O^{\bullet\bullet}$–In′ clusters in $Ba(Zr_{0.9}In_{0.1})O_{3-\delta}$ post-annealed at 1300 °C, which is 380 degrees below the sintering temperature (1680 °C), sufficiently for 100 h by using atomic-scale STEM in high-angle annular dark-field (HAADF) and annular bright-field (ABF) modes. HAADF-STEM provides Z-contrast images where the intensity proportionally depends on the average atomic number, Z, of columns and ABF-STEM can image atomic columns consisting of light elements.[22] Consequently, the combined HAADF- and ABF-STEM is a suitable tool for direct visualization of both In ($Z = 49$) substituted for the Zr ($Z = 40$) site and vacancies in the O site. Figure 3 shows atomic-scale STEM images simultaneously acquired in both HAADF and ABF modes in the [100] projection. As indicated by a red arrow in the HAADF image (upper left), this Zr column is observed to have a higher intensity than that of other Zr columns, demonstrating the presence of In. Oxygen columns are clearly identified with substantial contrast in the ABF image (lower right). Although it is usually difficult to precisely define the Z- and occupancy-dependent proportionality in ABF-STEM, our ABF image simulations verify that sufficiently detectable contrast reduction in the O columns is induced by vacancies (see the Supporting Information, Figure S8 for details). As denoted by a yellow arrow in the ABF image (lower right) and further clarified in the inverse ABF image in color (upper right) in Figure 3, we indeed observed the O column showing a sig-

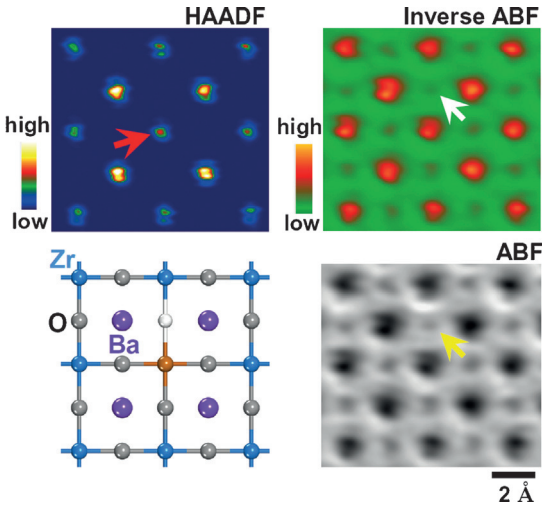

Figure 3. Set of HAADF- and ABF-STEM images in the [100] projection of $Ba(Zr_{0.9}In_{0.1})O_{3-\delta}$ post-annealed at 1300 °C for 100 h after sintering. The atomic columns in ABF mode are presented with black contrast. Therefore, the inverse ABF image, where the black and white contrasts are inverted, is demonstrated along with the original ABF image to clarify the intensity reduction by an oxygen vacancy, as denoted by white and yellow arrows in each of the images. The red arrow in the HAADF image indicates a Zr column with a higher intensity, proving the substitution by In, as illustrated in the two-dimensional atomic array.

nificantly reduced contrast next to the In-containing columns in many cases in the STEM analysis. The appearance of brighter intensity in a Zr column in the HAADF mode and reduced contrast in an O column neighboring the brighter Zr column in the ABF mode directly indicates the presence of $V_O^{\bullet\bullet}$–In′ clustering. Another series of STEM images is included in the Supporting Information, Figure S9 for confirmation.

To correlate the theoretical calculation results shown in Figures 1 and 2 with the real proton conduction behavior, we prepared two different kinds of polycrystalline samples of $Ba(Zr_{0.9}In_{0.1})O_{3-\delta}$, $Ba(Ce_{0.9}In_{0.1})O_{3-\delta}$, $Ba(Zr_{0.9}Y_{0.1})O_{3-\delta}$, and $Ba(Zr_{0.9}Sc_{0.1})O_{3-\delta}$, respectively: as-sintered specimens (1680 °C for the zirconate and 1400 °C for the cerate) and specimens subjected to post-annealing at lower temperatures after sintering (1300 °C for the zirconate and 1150 °C for the cerate) to induce $V_O^{\bullet\bullet}$–A′ clustering. The bulk proton conductivity of each sample was measured by using impedance spectroscopy. Proton trapping is much more dominant at relatively low temperature.[16] Thus, most measurements were first carried out below 300 °C, where many electrochemical devices based on proton conduction are operated.[23] Figure 4 compares the impedance results measured at 160 °C before and after post-annealing for each of the samples. While the bulk impedance shows a marginal change in $Ba(Zr_{0.9}Y_{0.1})O_{3-\delta}$ (Figure 4c) and also no observable variation in $Ba(Zr_{0.9}Sc_{0.1})O_{3-\delta}$ (Figure 4d), a substantially reduced diameter of the arc at high frequencies in each of the Nyquist plots in $Ba(Zr_{0.9}In_{0.1})O_{3-\delta}$ and $Ba(Ce_{0.9}In_{0.1})O_{3-\delta}$ (Figure 4a,b) is clearly identified in the post-annealed samples. This provides compelling evidence of significant enhancement of the proton conductivity. In particular, the nearly two-fold

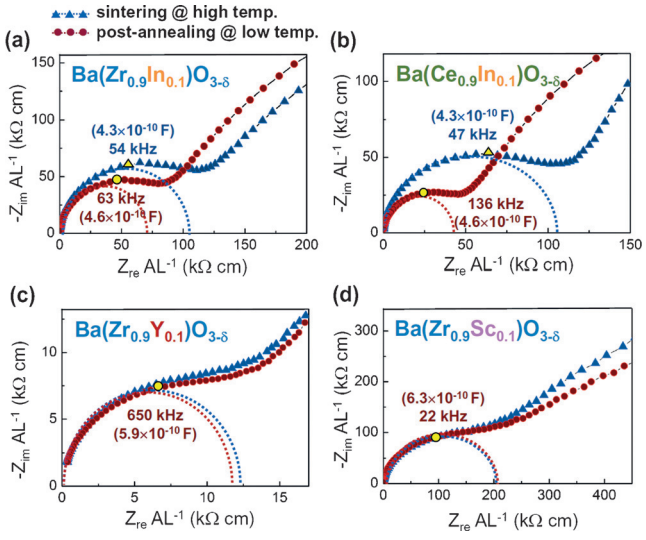

Figure 4. Nyquist plots for the AC impedance measurements at 160}C. Remarkable decreases in bulk impedance by post-annealing after sintering are readily identified by the diameter reduction of the high-frequency arcs in both a) $Ba(Zr_{0.9}In_{0.1})O_{3-\delta}$ and b) $Ba(Ce_{0.9}In_{0.1})O_{3-\delta}$, as denoted by broken curves of the impedance spectra. In contrast, no significant variation in impedance by post-annealing in c) $Ba(Zr_{0.9}Y_{0.1})O_{3-\delta}$ and d) $Ba(Zr_{0.9}Sc_{0.1})O_{3-\delta}$ before and after post-annealing is observed.

increment of conductivity observed in post-annealed $Ba(Ce_{0.9}In_{0.1})O_{3-\delta}$ accomplished by a simple annealing process is notable. Using image analysis with scanning electron microscopy (SEM) and a quantitative electron probe microanalysis (EPMA), we also confirmed that neither the average size nor the chemical composition of single grains was affected by post-annealing (Supporting Information, Figures S10 and S11, Tables S3 and S4). Consequently, the significant reduction in bulk impedance by post-annealing shown in In-doped $BaZrO_{3-\delta}$ and $BaCeO_{3-\delta}$ in Figure 4 is in excellent agreement with the reduction in $OH^{\bullet}$–In′ binding energy when $V_O^{\bullet\bullet}$ is engaged near In′, as predicted by the DFT calculations in Figure 2. The reduction of the bulk impedance by post-annealing was also consistently verified in the case of $Ba(Ce_{0.85}In_{0.15})O_{3-\delta}$ with a higher concentration of acceptor dopants (Supporting Information, Figure S12), showing that post-annealing has general implications with regard to the proton conduction enhancement irrespective of the doping level.

If the binding characteristics between $OH^{\bullet}$ and In′ become weak, the energy barrier for proton migration should be reduced together with the increment of proton conductivity. We thus determined the activation energies (E_A) of migration by plotting the variation of proton conductivity as a function of temperature. Figure 5 shows the Arrhenius plots of proton

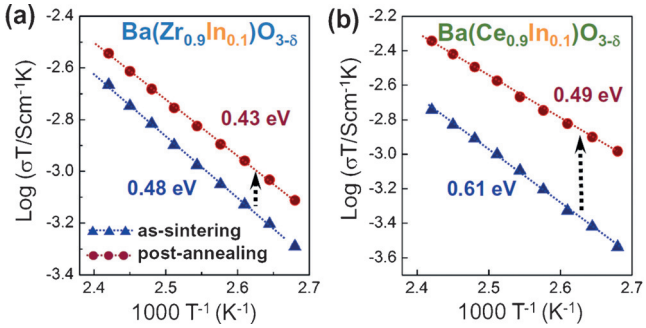

Figure 5. Arrhenius plots of proton conductivities measured by impedance spectroscopy. In addition to the enhancement of proton conductivities, the activation energies of proton migration are reduced by the post-annealing process in both a) $Ba(Zr_{0.9}In_{0.1})O_{3-\delta}$ and b) $Ba(Ce_{0.9}In_{0.1})O_{3-\delta}$. The consistent reduction of the activation barrier in two independent perovskite oxides is noted, offering critical evidence that proton trapping is efficiently alleviated.

conductivities in a temperature range of 80–160 °C. The difference in slope of the linear fits between as-sintered and post-annealed samples is easily recognized in each of the plots, directly demonstrating the reduction of E_A, from 0.48 eV to 0.43 eV in $Ba(Zr_{0.9}In_{0.1})O_{3-\delta}$ and from 0.61 eV to 0.49 eV in $Ba(Ce_{0.9}In_{0.1})O_{3-\delta}$. This coherent reduction of E_A through post-annealing in two independent acceptor-doped perovskite oxides provides compelling evidence regarding the crucial role of oxygen vacancies in the efficient screening of an attractive interaction between protons and In by forming $V_O^{\bullet\bullet}$–In′ clusters. Post-annealing time-dependent behavior of the activation energy in $Ba(Ce_{0.9}In_{0.1})O_{3-\delta}$ is also provided in the Supporting Information, Figure S13, to consistently show

the activation energy variation. The Arrhenius plots of proton conductivities along with the values of E_A in $Ba(Zr_{0.9}Y_{0.1})O_{3-\delta}$ and $Ba(Zr_{0.9}Sc_{0.1})O_{3-\delta}$ are shown in the Supporting information, Figure S14.

It is worthwhile to mention that the temperature of post-annealing was not determined arbitrarily. To suppress the entropy influence and subsequently the random distribution of oxygen vacancies, lowering the annealing temperature is always preferred from a thermodynamic viewpoint. However, providing sufficient thermal energy is also necessary so that oxygen vacancies will easily diffuse toward acceptors for clustering by overcoming the activation barrier in the lattice. Therefore, there is an optimum intermediate range of temperature for post-annealing (Supporting Information, Figures S15 and S16).

In summary, we have demonstrated that proton trapping toward acceptors can be remarkably alleviated by forming $V_O^{\bullet\bullet}$–A′ clusters in $BaZrO_{3-\delta}$ and $BaCeO_{3-\delta}$. To make the clusters active for screening the attraction between A′ and $OH^{\bullet}$, it is preferred that the d orbitals in acceptors are weakly hybridized with the O 2p orbitals and consequently the valence electronic density of acceptors should not be seriously affected by the formation of oxygen vacancies. The present findings not only clarify the role and conditions of defect associations in improving proton conduction, but also emphasize the notable impact of electronic structure variations in dopants on the overall ionic transport behavior in perovskite oxides.

Acknowledgements

This work was supported by the National Research Foundation of Korea (NRF), grants no. 2014R1A4A1003712 (BRL Program) and 2013M3A6B1078874. H.S.K. and S.Y.C. were also financially supported by the End-Run Project by the Institute for Startup KAIST. The authors thank the referee for the valuable suggestions and discussion regarding the impedance analysis.

Keywords: defects · electronic structure · perovskite phases · proton conduction · vacancies

How to cite: *Angew. Chem. Int. Ed.* **2016**, *55*, 13499–13503
Angew. Chem. **2016**, *128*, 13697–13701

[1] D. M. Smyth, *The Defect Chemistry of Metals Oxides*, Oxford University Press, New York, **2000**.
[2] J. Maier, *Physical Chemistry of Ionic Materials: Ions and Electrons in Solids*, Wiley, New Jersey, **2004**.
[3] A. Rothschild, W. Menesklou, H. L. Tuller, E. Ivers-Tiffée, *Chem. Mater.* **2006**, *18*, 3651–3659.
[4] T. Norby, *Solid State Ionics* **1999**, *125*, 1–11.
[5] K. D. Kreuer, *Solid State Ionics* **1999**, *125*, 285–302.
[6] H. G. Bohn, T. Schober, *J. Am. Ceram. Soc.* **2000**, *83*, 768–772.
[7] K. D. Kreuer, *Annu. Rev. Mater. Res.* **2003**, *33*, 333–359.
[8] Y. Yamazaki, R. Hernandez-Sanchez, S. M. Haile, *Chem. Mater.* **2009**, *21*, 2755–2762.
[9] L. Buannic, F. Blanc, D. S. Middlemiss, C. P. Grey, *J. Am. Chem. Soc.* **2012**, *134*, 14483–14498.
[10] a) S. Tao, J. T. S. Irvine, *Adv. Mater.* **2006**, *18*, 1581–1584; b) E. Fabbri, L. Bi, D. Pergolesi, E. Traversa, *Adv. Mater.* **2012**, *24*, 195–208; c) C. Duan, J. Tong, M. Shang, S. Nikodemski, M. Sanders, S. Ricote, A. Almansoori, R. O'Hayre, *Science* **2015**, *349*, 1321–1326.
[11] T. Norby, M. Widerøe, R. Glöckner, Y. Larring, *Dalton Trans.* **2004**, 3012–3018.
[12] T. Matzke, U. Stimming, C. Karmonik, M. Soetratmo, R. Hempelmann, F. Güthoff, *Solid State Ionics* **1996**, *86–88*, 621–628.
[13] M. S. Islam, P. R. Slater, J. R. Tolchard, T. Dinges, *Dalton Trans.* **2004**, 3061–3066.
[14] P. G. Sundell, M. E. Björketun, G. Wahnström, *Phys. Rev. B* **2006**, *73*, 104112.
[15] M. E. Björketun, P. G. Sundell, G. Wahnström, *Phys. Rev. B* **2007**, *76*, 054307.
[16] Y. Yamazaki, F. Blanc, Y. Okuyama, L. Buannic, J. C. Lucio-Vega, C. P. Grey, S. M. Haile, *Nat. Mater.* **2013**, *12*, 647–651.
[17] K. D. Kreuer, S. Adams, W. Münch, A. Fuchs, U. Klock, J. Maier, *Solid State Ionics* **2001**, *145*, 295–306.
[18] I. Oikawa, H. Takamura, *Chem. Mater.* **2015**, *27*, 6660–6667.
[19] R. S. Mulliken, *J. Chem. Phys.* **1955**, *23*, 1833–1840.
[20] S.-Y. Chung, Y.-M. Kim, S.-Y. Choi, J.-G. Kim, *J. Am. Chem. Soc.* **2013**, *135*, 7811–7814.
[21] R. E. Cohen, *Nature* **1992**, *358*, 136–138.
[22] R. Ishikawa, E. Okunishi, H. Sawada, Y. Kondo, F. Hosokawa, E. Abe, *Nat. Mater.* **2011**, *10*, 278–281.
[23] a) A. Tomita, J. Nakajima, T. Hibino, *Angew. Chem. Int. Ed.* **2008**, *47*, 1462–1464; *Angew. Chem.* **2008**, *120*, 1484–1486; b) T. Hibino, K. Kobayashi, M. Nagao, S. Kawasaki, *Sci. Rep.* **2015**, *5*, 7903; c) A. Tomita, T. Hibino, M. Suzuki, M. Sano, *J. Mater. Sci.* **2004**, *39*, 2493–2497.

Received: April 20, 2016
Revised: June 22, 2016
Published online: August 16, 2016

